



Available online at www.sciencedirect.com

ScienceDirect

Geochimica et Cosmochimica Acta 328 (2022) 242–257

Geochimica et
Cosmochimica
Acta

www.elsevier.com/locate/gca

Controls on the magnitude of Ce anomalies in zircon

Matthew A. Loader ^{a,b,*}, Chetan L. Nathwani ^{b,a}, Jamie J. Wilkinson ^{a,b},
Robin N. Armstrong ^a

^a London Centre for Ore Deposits and Exploration (LODE), Department of Earth Sciences, Natural History Museum, Cromwell Road, London SW7 5BD, UK

^b Department of Earth Science and Engineering, Imperial College London, South Kensington Campus, Exhibition Road, London SW7 2AZ, UK

Received 15 June 2021; accepted in revised form 17 March 2022; Available online 22 March 2022

Abstract

Increases in the magnitude of positive Ce anomalies in zircons from igneous rocks are often interpreted to be controlled by progressive melt oxidation and have been used to provide evidence for the elevated redox state of magmas associated with porphyry Cu deposits. In this paper, we test this idea by comparing trace element compositions of zircons from the Resolution porphyry Cu-Mo deposit, Arizona, with numerical models of melt Ce systematics and zircon-melt trace element partitioning. We show that although Ce anomalies in Resolution zircons (estimated by the chondrite-normalised ratio of Ce and Nd) may increase by over an order of magnitude throughout the period of zircon crystallisation, oxybarometric estimates in fact indicate a constant melt redox during this time. We employ a Monte Carlo approach to model the evolution of the Ce anomaly in zircon as a function of temperature, fO_2 , and melt composition, and compare our model against literature zircon data from chemically well-constrained volcanic rocks. We find that large increases in the magnitude of the Ce anomaly can be reproduced by cooling at fixed oxidation state and that this effect is magnified by increasing the melt Ce/Nd ratio, which can be driven by the co-crystallisation of amphibole, apatite and especially titanite. Increases in melt oxidation state are not sufficient to explain high positive Ce anomalies in zircons from some hydrous, oxidised volcanic and hypabyssal rocks, which additionally require a combination of titanite co-crystallisation and low crystallisation temperature. We therefore caution against the interpretation of zircon Ce anomalies solely in the context of melt fO_2 variation.

© 2022 The Authors. Published by Elsevier Ltd. This is an open access article under the CC BY license (<http://creativecommons.org/licenses/by/4.0/>).

Keywords: Zircon; Cerium; Porphyry Cu; Magma; Redox

1. INTRODUCTION

Zircon has proven to be an essential tool in unravelling the complex petrogenesis of igneous and metamorphic rocks. In addition to its widespread use in geochronological studies (e.g., [Davis et al., 2003](#)), zircon also provides a chemical record of its crystallisation environment due to the partitioning of many trace elements into its structure,

including the rare earth elements (REEs), Y, Ti, Hf, Th and U ([Hoskin and Schaltegger, 2003](#)). Due to its robustness and resistance to alteration and diffusive re-equilibration ([Cherniak and Watson, 2003](#)), zircon is particularly useful in understanding the petrogenesis of igneous rocks where the chemical context has been compromised by weathering and erosion (i.e., detrital zircons; [Morton et al., 2015](#)) or strong chemical alteration in magmatic-hydrothermal systems. One recent application of zircon chemistry is in tracking the evolution of magmas associated with porphyry Cu-Mo-Au ore deposits. These systems comprise large volumes of metal sulphide-bearing, hydrothermally altered rock, in which the main ore-forming

* Corresponding author at: London Centre for Ore Deposits and Exploration (LODE), Department of Earth Sciences, Natural History Museum, Cromwell Road, London SW7 5BD, UK.

E-mail address: matthew.loader@nhm.ac.uk (M.A. Loader).

components (metals, sulphur, chlorine, hydrothermal fluids) are derived from primarily subduction-related, intermediate-felsic magmas (Seedorff et al., 2005; Sillitoe, 2010). The ‘fertile’ magmas that are predisposed to form such deposits are thought to originate by extensive fractional crystallisation in the deep crust under oxidising and hydrous conditions, where amphibole and garnet dominate the fractionating assemblage and plagioclase is suppressed. This imparts a characteristic whole rock trace element signature (e.g., low Y, high Eu and Sr; Richards, 2011; Loucks, 2014). However, this may be modified by the later hydrothermal alteration that is ubiquitous in these systems. Thus, zircon has received attention as it may preserve an intact record of these igneous signatures and thereby constitute a useful tool for porphyry deposit exploration (e.g., Pizarro et al., 2020).

Two features of porphyry zircon chemistry which are a particular focus of study are the anomalous concentrations of Eu and Ce. Unlike other REEs, which are exclusively trivalent, Ce and Eu may also exist as Ce^{4+} and Eu^{2+} in terrestrial magmas (Burnham and Berry, 2014; Burnham et al., 2015). Due to its similar ionic radius and charge to Zr^{4+} , Ce^{4+} is considerably more compatible in zircon than Ce^{3+} , leading to anomalously high Ce in zircon (generating a positive Ce anomaly in REE patterns). Conversely, Eu^{2+} is much less compatible than Eu^{3+} , meaning that zircons commonly display negative Eu anomalies. The magnitude of these anomalies are normally expressed as the ratio of measured Ce or Eu to the concentration expected if these elements behaved similarly to their neighbouring cations, denoted by Ce^* and Eu^* (where $\text{Ce}^* = \sqrt{(\text{La}_N \times \text{Pr}_N)}$ and $\text{Eu}^* = \sqrt{(\text{Sm}_N \times \text{Gd}_N)}$ and the subscript N means values are chondrite normalised; Sun and McDonough, 1989).

Recent studies have noted that the values of Eu/Eu^* and Ce/Ce^* in zircons from porphyry-related magmas are, on average, higher than those in typical arc magmas (e.g., Lu et al., 2016; Loader et al., 2017; Pizarro et al., 2020). Furthermore, these values have been shown to increase progressively with fractionation within a population of zircons from a single rock (e.g., Kobylnski et al., 2020), and between successive intrusions leading up to a porphyry ore-forming event (e.g., Ballard et al., 2002; Dilles et al., 2015). Experimental studies have shown that both Ce/Ce^* and Eu/Eu^* increase with melt oxygen fugacity ($f\text{O}_2$; Burnham and Berry, 2012; Trail et al., 2012; Smythe and Brenan, 2016). This has potential metallogenetic significance: at higher $f\text{O}_2$, sulphur is present in magmas as sulphate (S^{6+}), whereas in more reduced magmas (below the fayalite magnetite quartz (FMQ) redox buffer) sulphide (S^{2-}) dominates (Jugo et al., 2010), which saturates more easily to form an immiscible sulphide melt which strongly partitions Cu (e.g., Patten et al., 2013). This can lead to the loss of both sulphur and metals from the melts, thereby potentially reducing their ore-forming potential. Taken together, these observations have been used as evidence that: (1) porphyry magmas are more oxidised than typical arc magmas ($>\Delta\text{FMQ} + 2$; Sun et al., 2015); and (2) that $f\text{O}_2$ increases through successive intrusions leading up to mineralisation, and therefore may be a controlling factor in ore formation.

However, the magnitudes of zircon Eu/Eu^* and Ce/Ce^* are unlikely to solely depend on melt $f\text{O}_2$. For example, Loader et al. (2017) demonstrated that high Eu/Eu^* values in porphyry zircons can be generated by the onset of titanite crystallisation, which may be induced by changes in melt composition and temperature as well as increases in oxidation state (Kohn, 2017). This interpretation has been echoed in studies of zircon from other porphyry systems, where phases such as apatite, plagioclase, and amphibole have also been suggested to influence coeval melt, and thence zircon Eu anomalies (Rezeau et al., 2019; Nathwani et al., 2021). Similarly, zircon Ce anomalies are likely to reflect a more complex set of physical and chemical processes beyond simply recording changes in oxidation state. For example, Loucks et al. (2018) showed, with reference to experimental and natural zircons (Colombini et al., 2011; Burnham and Berry, 2012), that the relative partitioning of Ce^{4+} over Ce^{3+} in zircon increases as melt temperature decreases, meaning the overall partitioning of Ce in zircon can be temperature sensitive (Trail et al., 2012) and therefore also linked to the degree of melt differentiation. Furthermore, Smythe and Brenan (2015) showed that $\text{Ce}^{4+}/\text{Ce}_{\text{melt}}^{3+}$, higher values of which will lead to larger positive zircon Ce anomalies, is controlled by temperature, melt water content, degree of melt polymerisation, and oxidation state. Finally, the unequal fractionation of REE due to the co-crystallisation of titanite and other phases (e.g., Wotzlaw et al., 2013; Szymanowski et al., 2017) may affect estimates of the magnitude of Ce^* insofar as these estimates are based on extrapolations from other REEs.

In this paper, we attempt to reconcile these competing variables in a model which can reproduce trends in the Ce anomalies of zircons from diverse igneous systems. We use a Monte Carlo numerical modelling approach to evaluate the sensitivity of the Ce anomaly to a variety of parameters. We compare our model results to new zircon data from one of the world’s largest porphyry systems, the Resolution porphyry Cu-Mo deposit, Arizona, as well as literature zircon data from several volcanic systems.

2. METHODS

2.1. Sample details

Fifteen intrusive rock samples were collected for this study from the Resolution district, both from drill core within the deposit and surface samples from regional intrusions. Twelve of the samples are from felsic dykes and stocks in the Resolution system. These contain a phenocryst assemblage of feldspar, biotite and quartz in a groundmass of the same phases (Fig. 1a, b) and have been intensely hydrothermally altered, destroying much of the original igneous mineralogy. An initial stage of potassic alteration led to the replacement of all plagioclase (including the phenocrysts) with K-feldspar (Fig. 1a) and some rocks in shallow parts of the deposit were affected by a subsequent stage of phyllitic alteration which replaced the K-feldspar with sericitic and the biotite with sulphides (Fig. 1b) and advanced argillic alteration characterised by pyrophyllite, topaz, and dickite (Hehnke et al., 2012). All of the Resolution

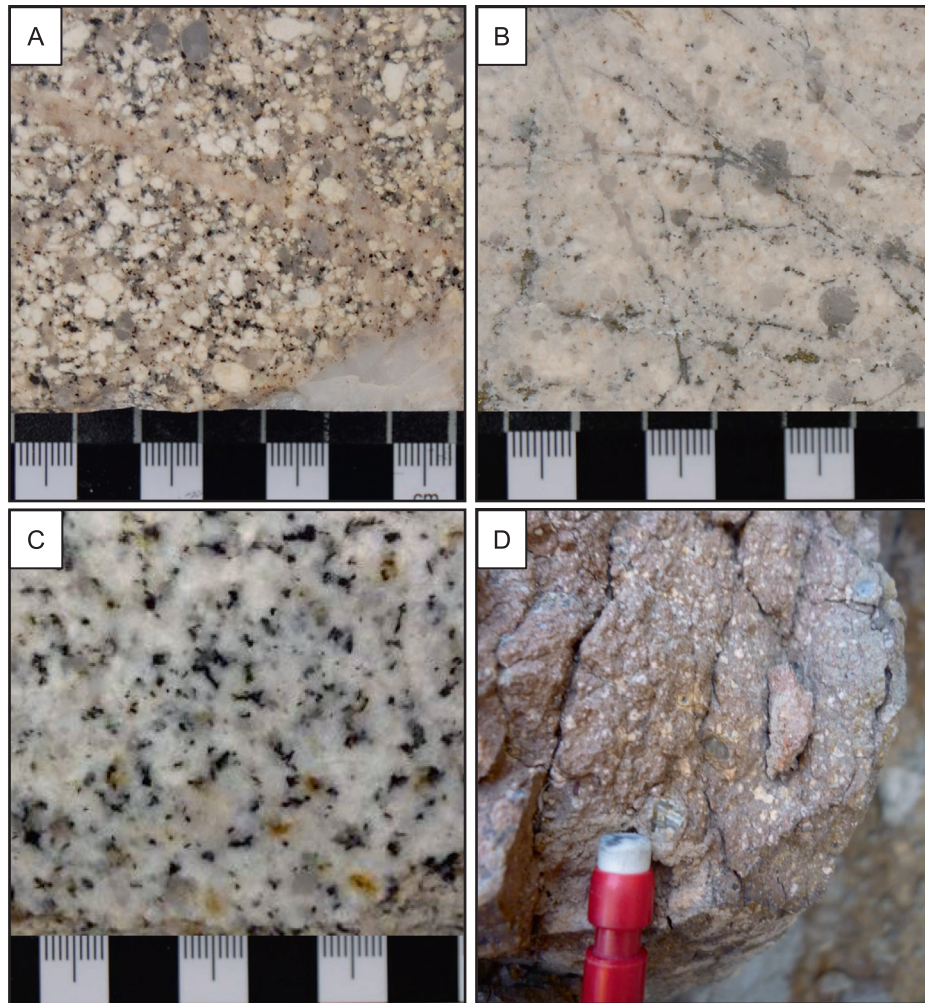


Fig. 1. Representative images of studied samples. (A) Potassic alteration and (B) sericitic alteration in a crowded rhyodacite porphyry from the Resolution deposit. Note the preservation of rounded quartz 'eyes' in sericitically altered rocks. (C) the main phase of the Schultze Granite; and (D) felsic porphyritic dyke from the Apache Leap intrusions.

intrusions are considered to predate the main mineralisation event.

Two samples were selected from the Schultze Granite – a batholith considered to be the 'parent' pluton to the Resolution intrusions, which crops out ~8 km northeast of the Resolution deposit. The granite comprises quartz, plagioclase, megacrystic K-feldspar, and biotite, with accessory apatite, magnetite, and zircon (Fig. 1c). One minor felsic dyke was sampled near the town of Superior to the west of Resolution. This intrusion was previously dated by Seedorff et al., 2019 to 66.2 ± 1.0 Ma, and comprises sparse feldspar, quartz, and subordinate chloritised amphibole phenocrysts in a fine-grained, weakly altered groundmass (Fig. 1d). A sample list is given in the Appendix. Further details of the samples are available in Loader (2017).

2.2. Mineral separation

Samples were crushed and sieved through a 300 μm mesh. The fine sand fraction was then run through a centrifuge with lithium metatungstate to remove grains with

density $< 2.8 \text{ g cm}^{-3}$. Residual heavy components were dried and run through a Franz magnetic separator at varying current (0.5 A, 1.0 A and 1.6 A). Zircons were separated from other minerals in the non-magnetic fraction by diiodomethane liquid. Once separated, zircons were picked under ethanol and mounted in 25 mm diameter epoxy resin blocks that were then polished to expose the midsections of the crystals.

2.3. Analytical techniques

Zircons were imaged and analysed during the same laboratory runs described by Loader et al. (2017) at the Imaging and Analysis Centre of the Natural History Museum, London, UK. Cathodoluminescence (CL) imaging of textures in zircon grains and identification of mineral inclusions were conducted using a Zeiss EVO scanning electron microscope (beam current 3.0 ± 0.3 nA, accelerating voltage 20 kV).

Trace element LA-ICP-MS analyses were carried out using an Agilent 7500cs quadrupole ICP-MS coupled to

an ESI New Wave UP193FX laser ablation system. Each analysis consisted of a 40 s measurement of instrument background, followed by a 95 s measurement during zircon ablation. A fluence of 2.5–3.0 J cm⁻² and a spot size of 30 µm were used. Primary and secondary standards for trace element analyses were NIST-612 and BCR-2 g, respectively. A stoichiometric value of Si (15.3 wt.%) was used as an internal standard to calibrate the mass of trace elements, and ExLAM2000 (Zacharias and Wilkinson, 2007) was used to process laser ablation data. Spectra were monitored for any chemical heterogeneity arising from accidental analyses of mineral or melt inclusions. Secondary standard (BCR-2 g) analyses, calibrated using the NIST-612 glass, reproduced the reference values with less than ±10% bias in all trace elements. Analytical precision, as determined by replicate analyses of BCR-2 g calibrated by NIST-612, was <4.5% relative standard deviation for all elements reported. See Loader et al. (2017) for accuracy and precision details.

2.4. Ti-in-zircon thermometry and zircon oxybarometry

Estimates of temperature were made using the Ferry and Watson (2007) calibration of the Ti-in-zircon thermometer, with a_{TiO_2} and a_{SiO_2} values of 0.7 and 1 respectively, in line with other estimates for zircons from porphyry systems (e.g., Chelle-Michou et al., 2014). The zircon oxybarometer of Loucks et al. (2020) was used to estimate melt $f\text{O}_2$.

3. RESULTS

3.1. Estimating Ce anomalies in zircon

First, we critically assessed existing methods used to quantify the Ce anomaly in zircon. Although most authors estimate the Ce anomaly geometrically using the geometric mean of La and Pr to estimate Ce*, this approach is not practical in zircon because both elements are present in such low concentrations that analyses very often fall below the limit of detection or are contaminated by accidental analysis of mineral inclusions. If the coexisting melt REE composition is known, Ce* may be estimated from partition coefficients using the lattice strain equation of Blundy and Wood (1994) (Fig. 2a; Trail et al., 2012), yet a coexisting melt is rarely available for natural zircons. In the absence of an equilibrium melt composition, internally consistent methods for estimating Ce* by extrapolating from measured REE heavier than Pr have been suggested (Loader et al., 2017) and improved upon (Zhong et al., 2019). We compared both methods with estimates for Ce* determined by lattice strain using natural zircon-matrix glass pairs and found that neither method was able to accurately reproduce the lattice strain value for Ce*, with very large discrepancies occurring in some cases (Fig. 2).

Here, as a practical and internally consistent simplification, we follow Chelle-Michou et al. (2014) and Lu et al. (2016) and use the ratio of chondrite-normalised Ce and Nd ($\text{Ce}/\text{Nd}_{\text{zrc}}$) to approximate the magnitude of Ce enrichment with respect to other light REE. This parameter was preferred for the purposes of this study because it can be

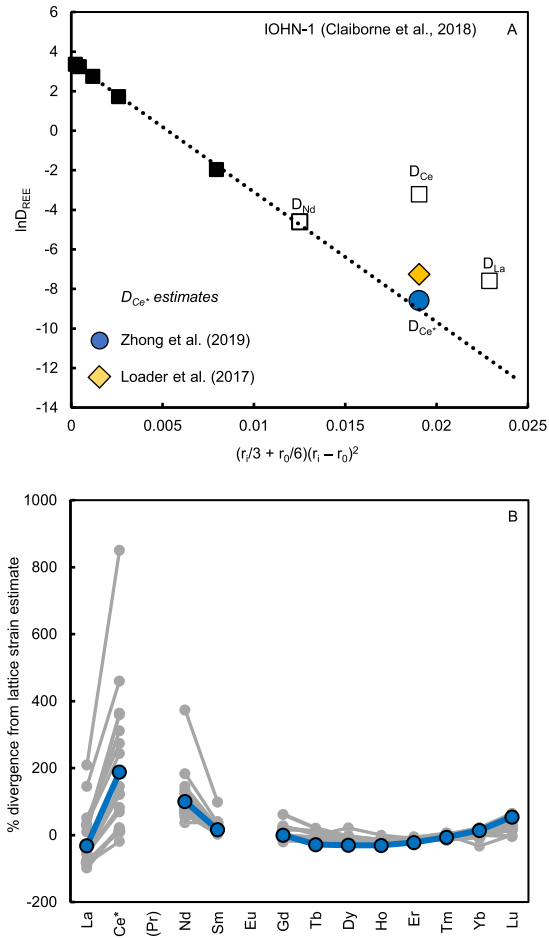


Fig. 2. Evaluating two methods for estimating Ce*, from Loader et al. (2017) and Zhong et al. (2019). (A) log-normalised measured zircon partition coefficients for transitional tholeiitic-alkalic sample IOHN-1 (Claiborne et al., 2018) versus the ionic radius parameter of the lattice strain equation (Blundy and Wood, 1994). The dotted line indicates a regression fitted to Ds for cations heavier than Nd (black squares) using the lattice strain equation. Ds for trivalent light REE (open squares) should fall on this regression line, as should the hypothetical D_{Ce*}; the deviation of D_{Ce} from the line for IOHN-1 is due to the presence of tetravalent Ce, whereas the deviation of D_{La} is likely due to very minor contamination during analysis. (B) Percentage error of REE concentrations in zircon estimated by the fitting technique of Zhong et al. (2019) calculated for published zircon-melt pairs. The comparison reference value is estimated using a lattice strain fitting technique (see Appendix for method). Sample IOHN-1 shown in (A) is highlighted in blue. Although the D_{Ce*} estimate of Zhong et al. (2019) appears to be a reasonably close match for the lattice strain model shown in (A) and is much closer than the estimate of Loader et al. (2017), the resultant estimate for Ce* in zircon deviates significantly relative to the reference value determined by lattice strain fitting. This confirms that Ce* cannot be accurately estimated, precluding the usefulness of Ce/Ce* as a parameter for zircon compositions.

calculated for literature data where not all the REE are reported, and because it is easier to model as only the concentrations and partition coefficients of two elements are needed. The ratio Ce/Nd_{zrc} correlates well with lattice

strain estimates for Ce/Ce* and is lower by approximately a factor of 10 (see Appendix).

3.2. Petrography and geochemistry

Zircons in all studied rocks range in size from <50 to ~300 µm, the largest being those from the Schultze Granite (Fig. 3c). Inherited cores of Proterozoic age are very common in zircons from all samples (cf. Seedorff et al., 2019); these are easily distinguished by irregular truncations in CL zoning patterns (Fig. 3) and are not considered further here. Care was taken when processing trace element data to

remove any mixed Proterozoic-Cretaceous analyses (distinguishable by low elemental U/Pb and Th/Pb ratios compared to normal rim values). Zircon rims often show narrow, concentric, oscillatory zoning (Fig. 3).

Zircons have chemical characteristics which indicate a dominant control of fractional crystallisation, with increasing Yb/Gd, and decreasing Eu/Eu*, Th/U, and Ti with increasing Hf content (Fig. 4). The ratio of Ce/Nd_{zrc} progressively increases from ~3 to 50 with decreasing Ti-in-zircon temperature (Fig. 5). Rather than reflecting an increase in Ce, which displays large scatter but on average remains nearly constant throughout fractionation, the

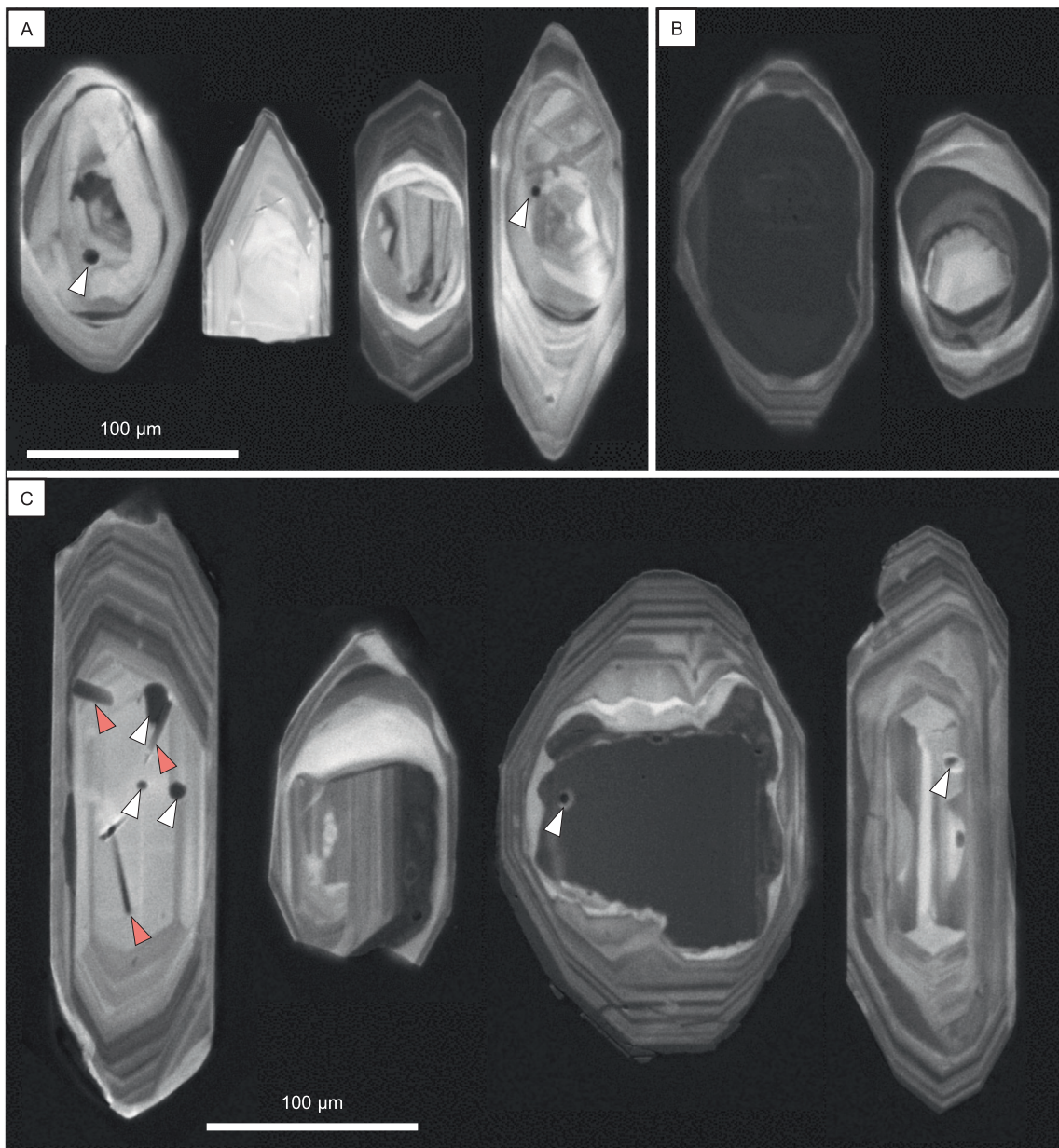


Fig. 3. Representative SEM-CL images of zircon in this study. Zircons from (A) Resolution intrusions; (B) Apache Leap felsic intrusions; and (C) Schultze Granite. Distinct Proterozoic cores and late-Cretaceous rims are identifiable in all examples, separated by an irregular resorption boundary, against which the zoning in the cores is truncated. White arrows indicate devitrified melt inclusions, and pink arrows highlight apatite inclusions.

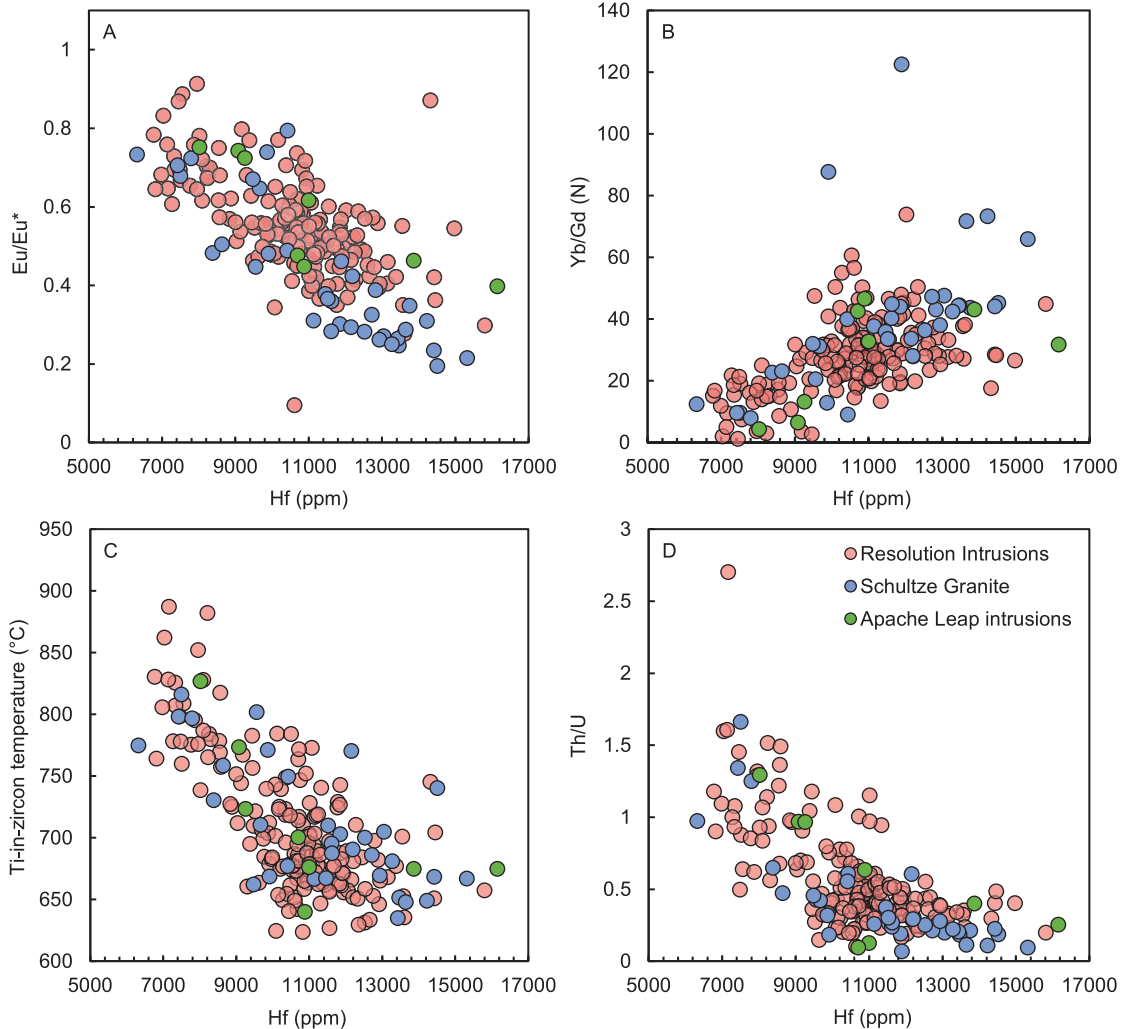


Fig. 4. The evolution of trace element compositions of zircons from the Resolution porphyry dykes and associated Laramide intrusions, with Hf concentration as a proxy for melt fractionation. (A) Eu/Eu* (B) Yb/Gd (normalised to chondrite values), (C) Ti-in-zircon temperatures and (D) Th/U ratios.

increase in Ce/Nd_{zrc} is due to the nearly two orders of magnitude decrease in Nd observed from 900 to 650 °C (from 13.5 to 0.2 ppm; Fig. 5b, c).

Estimates of melt *fO*₂ using the oxybarometer of Loucks et al. (2020) suggest a consistent oxidation state, buffered at approximately FMQ +2 (Fig. 6).

4. DISCUSSION

4.1. Controls on the magnitude of the Ce anomaly in zircon

As the ratio Ce/Ce* cannot be measured or estimated accurately in zircon, the following discussion uses and investigates Ce/Nd as a proxy for the Ce anomaly. The magnitude of Ce/Nd_{zrc} can be expressed as the quotient of the individual Nernst partitioning equations for each element:

$$\text{Ce}/\text{Nd}_{\text{zrc}} = \frac{D_{\text{Ce}}^{\text{zrc}} \times (X_{\text{Ce}}^{\text{melt}})_N}{D_{\text{Nd}}^{\text{zrc}} \times (X_{\text{Nd}}^{\text{melt}})_N} \quad (1)$$

where $D_{\text{Ce}}^{\text{zrc}}$ and $D_{\text{Nd}}^{\text{zrc}}$ are the zircon/melt partition coefficients for Ce and Nd, $X_{\text{Ce}}^{\text{melt}}$ and $X_{\text{Nd}}^{\text{melt}}$ are the melt concentrations for the same elements, and the subscript *N* denotes chondrite-normalised values (Sun and McDonough, 1989). Given that Ce⁴⁺ and Ce³⁺ have different charges and ionic radii and thus different partitioning behaviour (Blundy and Wood, 1994), $D_{\text{Ce}}^{\text{zrc}}$ varies as a function of the individual partition coefficients for Ce⁴⁺ and Ce³⁺, and their relative abundance in their melt. Following Wilke and Behrens (1999) and Aigner-Torres et al. (2007):

$$\frac{\text{Ce}^{4+}}{\text{Ce}^{3+} \text{melt}} = \frac{D_{\text{Ce}^{3+}}^{\text{zrc}} - D_{\text{Ce}}^{\text{zrc}}}{D_{\text{Ce}}^{\text{zrc}} - D_{\text{Ce}^{4+}}^{\text{zrc}}} \quad (2)$$

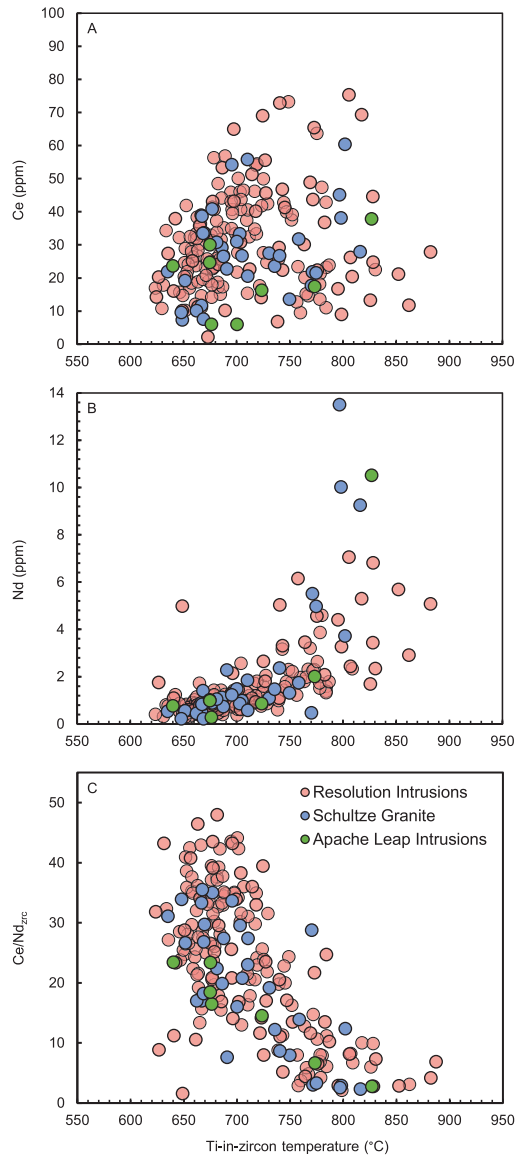


Fig. 5. Variations in zircon Ce/Nd, Ce, and Nd with Ti-in-zircon temperature. Increases in Ce/Nd with apparent cooling are largely driven by a decrease in Nd rather than an increase in Ce.

where $D_{\text{Ce}^{3+}}^{\text{zrc}}$ and $D_{\text{Ce}^{4+}}^{\text{zrc}}$ are the zircon/melt partition coefficients for Ce^{3+} and Ce^{4+} . Consequently, to model the magnitude of the Ce anomaly using Eq. (1), the individual partition coefficients for Ce^{4+} and Ce^{3+} and the ratio of both species in the melt must be estimated.

Studies of natural zircon-melt pairs have shown that for compatible REEs, $D_{\text{REE}^{3+}}^{\text{zrc}}$ values are inversely proportional to temperature (i.e., REE^{3+} partition more strongly into zircon at lower temperature; Claiborne et al., 2018), although the effect is significantly diminished as the cation radius, r_i , diverges from the ideal site radius, r_0 . For zircon, r_0^{3+} (~0.94 Å; e.g., Colombini et al., 2011) is much smaller than $r_{\text{Ce}^{3+}}$ or $r_{\text{Nd}^{3+}}$ (1.143 and 1.109 Å respectively). Consequently, estimates of $D_{\text{Ce}^{3+}}^{\text{zrc}}$ and $D_{\text{Nd}^{3+}}^{\text{zrc}}$ show no clear relationship with temperature (see Appendix), likely varying

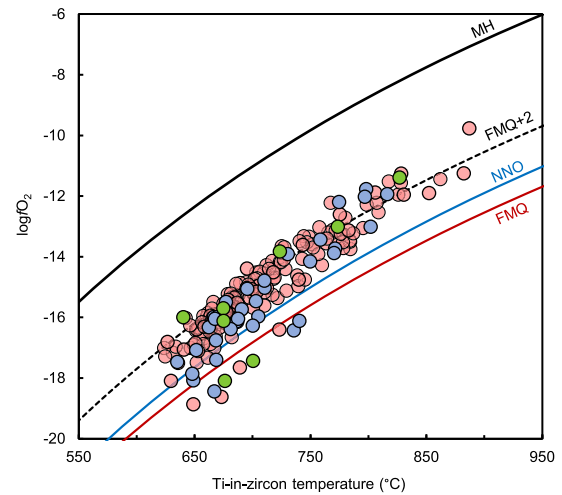


Fig. 6. Log oxygen fugacity ($\log O_2$) versus Ti-in-zircon temperature for the zircons from this study. $\log O_2$ was calculated using the zircon oxybarometer of Loucks et al. (2020). The fayalite-magnetite-quartz (FMQ), nickel-nickel oxide (NNO), and magnetite-hematite (MH) redox buffers are shown for reference. Most fO_2 estimates are two log units above FMQ (FMQ +2). Symbols as in Fig. 5.

within the error of the analyses. On the other hand, Ce^{4+} has the same charge and a sufficiently similar ionic radius ($r_{\text{Ce}^{4+}} = 0.97$) to the ideal tetravalent cation ($r_0^{4+} \approx 0.84$; Colombini et al., 2011), so Ce^{4+} partitions much more strongly into zircon at lower temperature (Fig. 7). This means that all other things being equal (i.e., fixed melt composition, relative fO_2 , and $\text{Ce}^{4+}/\text{Ce}_{\text{melt}}^{3+}$ ratio), the magnitude of the Ce anomaly in zircon is expected to increase with decreasing temperature (c.f. Loucks et al., 2018). However, during the period of zircon crystallisation, the melt composition, fO_2 , and melt $\text{Ce}^{4+}/\text{Ce}^{3+}$ ratio may vary considerably. Smythe and Brenan (2015) experimentally determined a relationship between $\text{Ce}^{4+}/\text{Ce}_{\text{melt}}^{3+}$ and melt oxidation state, temperature, water content, and degree of polymerisation:

$$\ln \left[\frac{x_{\text{Ce}^{4+}}^{\text{melt}}}{x_{\text{Ce}^{3+}}^{\text{melt}}} \right] = \frac{1}{4} \ln fO_2 + \frac{13136}{T(K)} - 2.064 \cdot NBO/T - 8.878 \cdot xH_2O - 8.955 \quad (3)$$

where T is temperature in Kelvin, NBO/T is the ratio of non-bridging oxygens to tetrahedral (network-forming) cations, and xH_2O is the mole fraction of water in the melt. This relationship predicts increases in $\text{Ce}^{4+}/\text{Ce}_{\text{melt}}^{3+}$ with increasing melt fO_2 , and with decreasing temperature, xH_2O , and NBO/T . Similar dependences have been reproduced in experiments by Burnham and Berry (2014) except for NBO/T , which was found to have the opposite effect on $\text{Ce}^{4+}/\text{Ce}_{\text{melt}}^{3+}$ in experiments without alkalis in the starting composition. The importance of melt alkali abundance on Ce speciation (see Cicconi et al., 2021 for review) makes the Smythe and Brenan (2015) experiments more applicable to late-stage felsic melts typically in equilibrium with zircon.

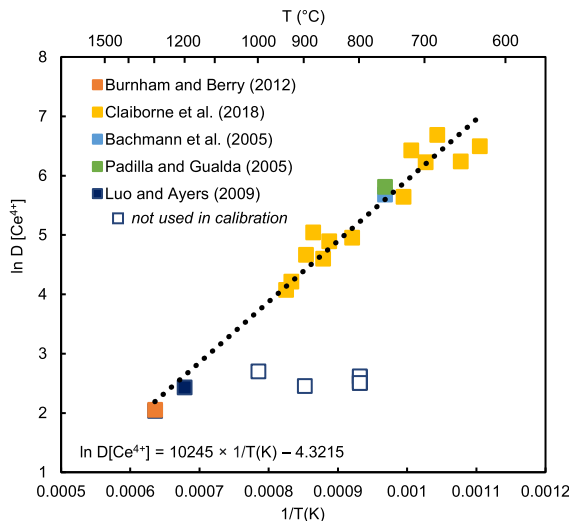


Fig. 7. Plot illustrating the strong correlation between $\ln D_{\text{Ce}^{4+}}^{\text{zrc}}$ and temperature for published natural and experimental zircon-melt pairs ($R^2 = 0.96$). Open symbols from Luo and Ayers (2009) were not used in the regression due to disequilibrium conditions in these lower temperature experiments.

Overall, the Ce anomaly is dependent on a multitude of factors that are rarely considered when interpreting zircon geochemical data. To assess the importance of these parameters in controlling Ce anomalies in natural zircons, we developed a numerical model which simulates $\text{Ce}/\text{Nd}_{\text{zrc}}$ as a function of $f\text{O}_2$, temperature and melt composition. Our model uses a Monte Carlo approach where parameters are varied stochastically within realistic bounds. $\text{Ce}^{4+}/\text{Ce}^{3+}$ is calculated using Eq. (3) by varying $f\text{O}_2$ and NBO/T as a function of the independent variable, temperature. We assumed water-saturated conditions at 200 MPa to fix the melt water content at 6 wt.% ($x_{\text{H}_2\text{O}} = 0.1866$; Newman and Lowenstern, 2002). We parameterised NBO/T as a function of temperature using a compilation dataset of experimental glasses equilibrated at ~200 MPa (Fig. 8). Using the calculated $\text{Ce}^{4+}/\text{Ce}^{3+}$ values and by rearranging equation (2), we estimated $D_{\text{Ce}}^{\text{zrc}}$. To do this, we used the relationship between $D_{\text{Ce}^{4+}}^{\text{zrc}}$ and temperature, described above, which was parameterised from a compilation of published zircon-melt pairs (Fig. 7). $D_{\text{Ce}^{4+}}^{\text{zrc}}$ and $D_{\text{Nd}}^{\text{zrc}}$ were kept constant and derived from published partition coefficients (Sano et al., 2002; Bachmann et al., 2005; Marshall et al., 2009; Padilla and Gualda, 2016; Claiborne et al., 2018). Finally, we varied the initial $\text{Ce}/\text{Nd}_{\text{melt}}$ ratio between 2 and 5, representing the natural range observed in rocks and matrix glasses in felsic volcanic systems (see Appendix). Details of the Monte Carlo simulations are available in the Appendix.

4.2. Effect of temperature

The model is consistent with earlier conclusions that temperature is a key variable controlling the magnitude of the Ce anomaly in zircon (Fig. 9). Zircons crystallising at high temperature (850–900 °C) have only small, positive

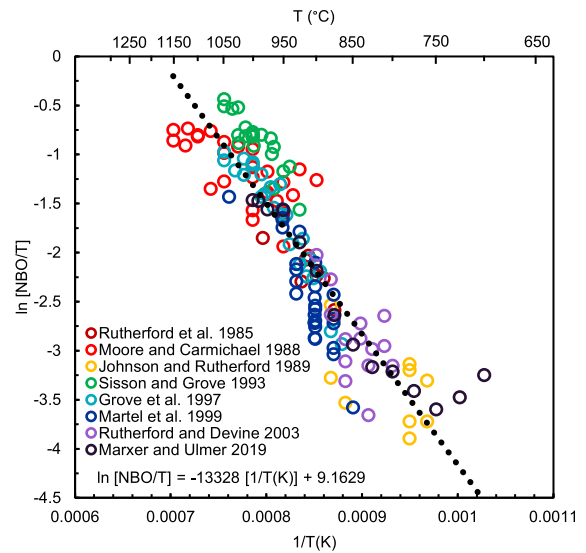


Fig. 8. $\ln \text{NBO}/\text{T}$ versus $1/\text{T}(\text{K})$ for experimental glasses from Rutherford et al. (1985), Moore and Carmichael (1988), Johnson and Rutherford (1989), Sisson and Grove (1993), Grove et al. (1997), Martel et al. (1999), Rutherford and Devine (2003), and Marquer and Ulmer (2019). These experiments were run at ~200 MPa. A best-fit line and corresponding equation are shown on the plot ($R^2 = 0.81$). This relationship defines the change in NBO/T with decreasing temperature in our model.

Ce anomalies ($\text{Ce}/\text{Nd}_{\text{zrc}} < 20$), even at high $f\text{O}_2$ and high initial $\text{Ce}/\text{Nd}_{\text{melt}}$ ($\Delta\text{FMQ} +2$; $\text{Ce}/\text{Nd}_{\text{melt}} = 5$; Fig. 9a). However, decreasing temperature is accompanied by a significant increase in zircon Ce anomaly for a fixed $\text{Ce}/\text{Nd}_{\text{melt}}$ and a buffered melt $f\text{O}_2$. This occurs due to: (a) the increase in melt $\text{Ce}^{4+}/\text{Ce}^{3+}$ with decreasing temperature; and (b) the increased overall compatibility of Ce in zircon due to the increase in $D_{\text{Ce}^{4+}}^{\text{zrc}}$ with decreasing temperature. Of these two processes, we find that increases in $D_{\text{Ce}^{4+}}^{\text{zrc}}$ play a more significant role in controlling the Ce anomaly than increasing melt $\text{Ce}^{4+}/\text{Ce}^{3+}$. This is because $D_{\text{Ce}^{4+}}^{\text{zrc}}$ increases by an order of magnitude between 950 and 650 °C (Fig. 7), causing a significant increase in Ce compatibility with cooling. Conversely, at a fixed oxidation state, $\text{Ce}^{4+}/\text{Ce}^{3+}$ only increases by a factor of approximately 1.5 between 1000 and 800 °C, below which it begins to decrease (Fig. 10). Although Eq. (3) predicts a strong increase in $\text{Ce}^{4+}/\text{Ce}^{3+}$ with decreasing temperature, an effect which is intensified by the concomitant decrease in NBO/T upon cooling (Fig. 8) which Eq. (3) shows would also act to increase $\text{Ce}^{4+}/\text{Ce}^{3+}$, both effects are moderated by the decrease in the absolute value of $\log\text{O}_2$ with decreasing temperature when following redox buffers (Fig. 6). Furthermore, the rate of NBO/T decrease during cooling slows exponentially (Fig. 8), whereas the rate of $\log\text{O}_2$ decrease with cooling continues to increase (Fig. 6), leading to a stabilisation and eventual decrease of $\text{Ce}^{4+}/\text{Ce}^{3+}$ at low temperature.

4.3. Effect of melt oxidation state

As expected, our model predicts that zircons crystallising from more oxidised melts have larger positive Ce anomalies

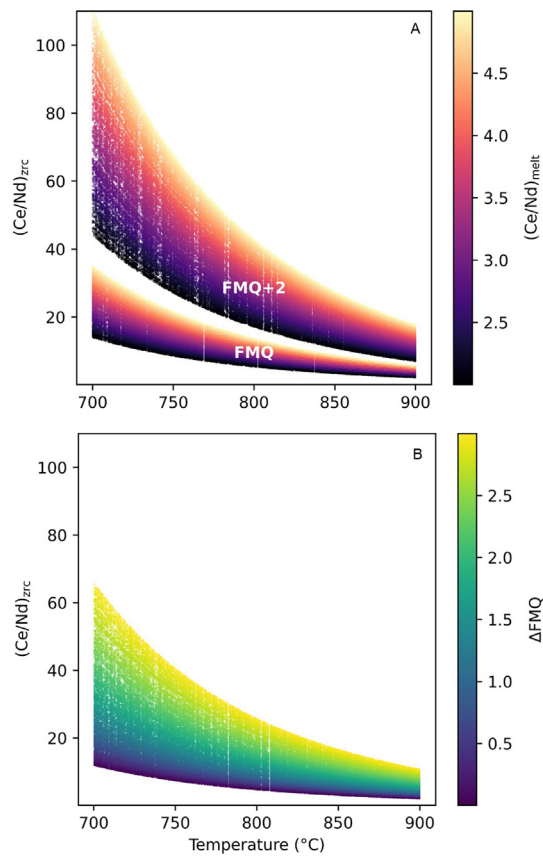


Fig. 9. Results of Monte Carlo simulations of the Ce/Nd_{zrc} ratio ($n = 10,000$). (A) two model runs at constant $f\text{O}_2$ (FMQ and FMQ +2), but variable melt chemistry (Ce/Nd_{zrc} = 2–5) and temperature. (B) fixed melt chemistry (Ce/Nd_{zrc} = 2) but variable $f\text{O}_2$ ($\Delta\text{FMQ}–\Delta\text{FMQ}+3$). These simulations highlight the relative importance of temperature, melt chemistry and $f\text{O}_2$ in governing the Ce anomaly in zircon. See text and supplementary information for a detailed discussion of the method.

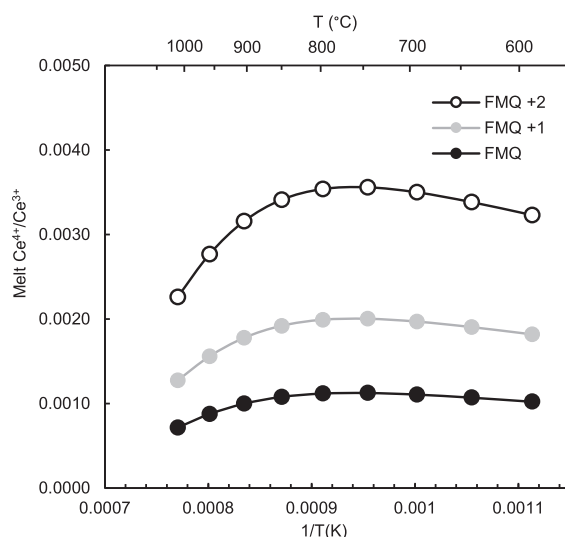


Fig. 10. Modelled melt Ce⁴⁺/Ce³⁺ as a function of the 1/T(K) for $f\text{O}_2$ values relative to the FMQ buffer (FMQ +0, +1, and +2) calculated using Eq. (3).

(Fig. 9a, b). This is because elevated melt $f\text{O}_2$ produces a higher Ce⁴⁺/Ce³⁺ at a given temperature, leading to increased partitioning of Ce relative to Nd in zircon. However, this does not mean that a trend of increasingly positive Ce anomalies with decreasing temperature reflects increasing melt oxidation state. When we fix the $f\text{O}_2$ in our model to match near-constant relative-to-buffer oxidation state during cooling of the Resolution system implied by the oxybarometer of Loucks et al. (2020), we observe a trend of increasing Ce/Nd_{zrc} with decreasing temperature which approximately matches the trend in the Resolution data (Fig. 11). In fact, even if the melt $f\text{O}_2$ is forced to decrease relative to redox buffers during cooling, increases in Ce/Nd_{zrc} may still result. These results show that increases in the size of positive Ce anomaly in zircon do not necessarily reflect increases in melt oxidation state and may in fact mask a modest melt reduction.

4.4. Effect of melt composition

Our model predicts that melt composition plays an important role in controlling the Ce/Nd ratio in zircon. For a fixed temperature and $f\text{O}_2$, increases in Ce/Nd_{melt} cause proportional increases in Ce/Nd_{zrc} (Fig. 9a), as described by Eq. (1). This effect is great enough that doubling Ce/Nd_{melt} within realistic bounds produces a greater increase in Ce/Nd_{zrc} than increasing the $f\text{O}_2$ by a log unit.

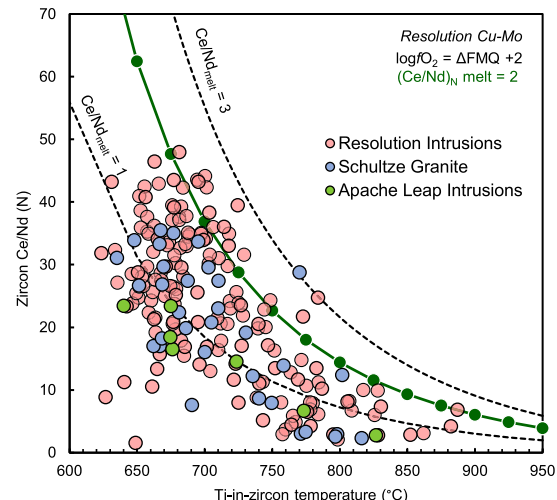


Fig. 11. Ce/Nd_{zrc} versus temperature for Resolution zircons, overlain by modelling results. For the model, $f\text{O}_2$ was held constant at $\Delta\text{FMQ} +2$ in line with oxybarometric estimates (see text). In the absence of matrix glass or melt inclusion data, melt chemistry was fixed at Ce/Nd_{melt} = 2, consistent with the Laramide porphyry rock chemistry (e.g., Lang and Titley, 1998). The effect of varying the Ce/Nd_{melt} parameter between 1 and 3 is shown by the dashed lines, indicating that much of the variability in the data can be explained by fluctuations in melt chemistry. This model highlights the effect of decreasing temperature on zircon Ce anomalies; the observed increase shows how melt oxidation is not required to explain elevated Ce anomalies in zircon. The model is also able to reproduce the spread of the zircon data if Ce/Ce* is considered instead of Ce/Nd (see Appendix).

An obvious question that follows is what processes can modify Ce/Nd_{melt} sufficiently to impact the Ce/Nd ratio in zircon? To assess these effects, we turn our attention to data from volcanic rocks with well-constrained melt chemistry. Although compilations of whole rock data show little variability in Ce/Nd_{rock} across the bulk compositional range (~1.5–2; see Appendix), zircon saturates well below the liquidus in intermediate to felsic magmas, after ~30–50% crystallisation (Schopha et al., 2017; Marxer and Ulmer, 2019), affording ample opportunity for residual melt compositions to diverge from bulk magma compositions by *in-situ* crystallisation. Increases in Ce/Nd_{melt} would be expected in this interval if magmas saturate phases that partition Nd more strongly than Ce; this is the case for both amphibole and titanite ($D_{Ce}/D_{Nd} \sim 0.3$; Bachmann et al., 2005; Nandedkar et al., 2016) and, to a lesser extent, apatite (~0.6; Sano et al., 2002). Conversely, plagioclase crystallisation would generate a lower Ce/Nd_{melt} ($D_{Ce}/D_{Nd} = 1.5$; Bachmann et al., 2005). Allanite, despite having very large partition coefficients for light REEs (D_{Ce} up to 2245; Klimm et al., 2008), has D_{Ce}/D_{Nd} ratios close to unity (~1.1–1.2) which, coupled with the very small abundance of allanite in some volcanic rocks (e.g., <50 ppm modal allanite in the early Bishop Tuff pumices; Hildreth and Wilson, 2007) means allanite is not able to strongly fractionate Ce from Nd, and thus will not be considered further.

A control of Ce/Nd_{melt} by titanite crystallisation is supported by interstitial glass data from titanite-bearing volcanic rocks which exhibit Ce/Nd_{melt} ratios that exceed bulk rock values by a factor of 2–3. For example, the dacitic Fish Canyon Tuff (Colorado, USA) contains both amphibole and titanite among other phenocrysts and has interstitial glass Ce/Nd values of 4–5, exceeding bulk rock values of ~2 (Bachmann et al., 2002). These inferred Ce/Nd_{melt} values may have been even higher prior to late-stage thermal rejuvenation and partial titanite remelting, which released REE back into the melt (Wotzlaw et al., 2013; see also Szymanowski et al., 2017). By contrast, the phenocryst assemblage of the Bishop Tuff (California, USA) is dominated by quartz, sanidine, and plagioclase, with close to no titanite and amphibole, and the Ce/Nd of both the interstitial glass and bulk rock are similar (~2–2.5; Hildreth, 1979; Chamberlain et al., 2015). In both volcanic systems, the interstitial glass chemistry is thought to represent the pre-eruptive residual melt composition that was dominantly controlled by the *in-situ* crystallisation and resorption of the phenocryst phases (Bachmann et al., 2002; Wotzlaw et al., 2013).

To assess the effect of titanite crystallisation on the magnitude of Ce/Nd_{zrc} we modelled the chemistry of zircons from the titanite-absent Bishop Tuff and Mt. Pinatubo 1991 dacite, and the titanite-bearing Fish Canyon, Peach Springs (Arizona, California, USA), and Kneeling Nun Tuffs (New Mexico, USA) and Highland Range volcanics (Nevada, USA) (data from Colombini, 2009; Reid et al., 2011; Pamukcu et al., 2013; Lu et al., 2016; Szymanowski et al., 2017; Nathwani et al., 2021). In the titanite-bearing tuffs, titanite crystallisation was simulated by increasing the Ce/Nd_{melt} linearly from 2 to 5, beginning at between

750 and 775 °C (the approximate saturation temperature of titanite in these systems; e.g., Olson et al., 2017; Szymanowski et al., 2017) and finishing at the approximate water-saturated granite solidus of 650 °C. For the Bishop Tuff zircons, the low Ce/Nd_{zrc} ratios at ~20 are easily reproducible by modelling at constant Ce/Nd_{melt} and varying fO_2 to match estimates from Fe-Ti oxides (Hildreth and Wilson, 2007; Fig. 12a). Similarly, the field of Pinatubo zircons is bisected by our models at constant Ce/Nd_{melt} but for higher oxidation state (FMQ +2.2; Evans and Scalliet, 1997). For the titanite-bearing volcanic rocks, our modelling shows that the higher oxidation state of these magmas compared to the Bishop Tuff (between ΔFMQ +2 and +4) is not sufficient on its own to explain the very high Ce/Nd_{zrc} ratios, which reach maximum values of between 100 and 200 (Fig. 12c–f). However, these high values can be attained if titanite co-crystallisation elevates Ce/Nd_{melt} to higher values. To attain such a high Ce/Nd_{zrc} due to increases in oxygen fugacity rather than changes in melt chemistry would require an increase in fO_2 of over 2 log units between 750 and 650 °C, far beyond what is predicted for these magmas. Although equivalently oxidised to the Kneeling Nun and Fish Canyon Tuffs but without co-crystallising titanite, zircons from the Pinatubo dacite have significantly lower Ce/Nd_{zrc} over a similar temperature range to the titanite-bearing volcanic systems (Fig. 12b).

In the case of the Resolution samples, a lack of matrix glass and melt inclusions due to intense hydrothermal alteration precludes knowledge of late-stage melt chemistry. A value of Ce/Nd_{melt} = 2, consistent with the chemistry of Laramide rocks associated with porphyry systems (Lang and Titley, 1998), can broadly reproduce the general trend of the Resolution zircons, and varying this value between 1 and 3 encompasses most of the variability in Ce/Nd_{zrc} (Fig. 11). The absence of titanite in these rocks is consistent with the near absence of Ce/Nd_{zrc} values exceeding ~50, a more common feature of low-temperature zircons from titanite-absent igneous rocks (e.g., Fig. 12a, b).

4.5. Zircon Ce anomalies in hydrous, oxidised magmas parental to porphyry Cu deposits

The occurrence of elevated, positive Ce anomalies in zircons from hydrous oxidised magmas, especially those associated with porphyry Cu deposits, is commonly ascribed to high oxidation states (Ballard et al., 2002; Chelle-Michou et al., 2014; Shen et al., 2015; Loader et al., 2017; Rezeau et al., 2019; Kobylinski et al., 2020; Viala and Hattori, 2021). However, recent oxybarometric estimates from igneous rocks from a range of porphyry deposits show a restricted range of fO_2 mostly between FMQ and FMQ +2.5 (Loucks et al., 2020), which are within the range of typical arc magmas (Jugo et al., 2010) and are significantly less oxidised than some lamprophyric magmas (e.g., Carmichael, 1991). These redox estimates do not vary significantly with decreasing temperature relative to redox buffers (Loucks et al., 2020), meaning that increases in Ce/Nd_{zrc} in such systems are unlikely to be due to increases in magma oxidation state alone. This is supported by our modelling, which shows that even in magmas where inde-

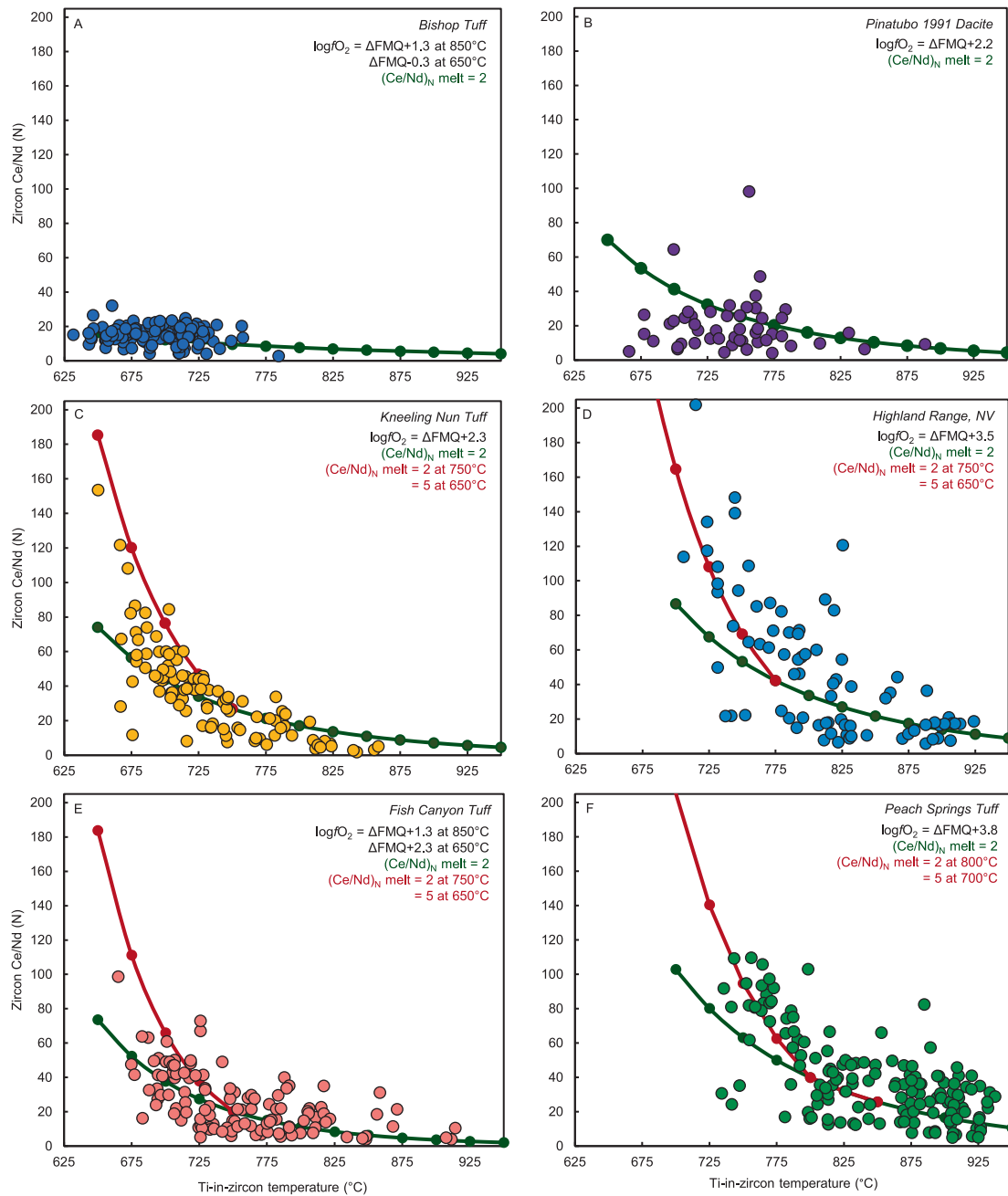


Fig. 12. Ce/Nd_{zrc} (chondrite normalised) versus temperature for zircons from several volcanic sequences; the titanite-absent Bishop Tuff, California (A) and Pinatubo 1991 dacite, Philippines (B), and the titanite-bearing Kneeling Nun Tuff, New Mexico (C), Highland Range volcanic sequence, Nevada (D) Fish Canyon Tuff, Colorado (E), and Peach Springs Tuff, Arizona (F). Model results are displayed in each case. For the Bishop Tuff and Pinatubo dacite, melt Ce/Nd is fixed at 2. For the other volcanic sequences, an additional red line shows how zircon Ce/Nd trends can be modelled better by including the onset of titanite crystallisation between 750 and 800 °C, after which the melt Ce/Nd was increased linearly from 2 to 5. For the Bishop and Fish Canyon Tuffs, fO_2 was fixed to match the change in fO_2 with temperature recorded by Fe-Ti oxides (Hildreth and Wilson, 2007; Whitney and Stormer, 1985; temperatures calculated using Ghiorso and Evans, 2008). For the Pinatubo dacite, the experimental estimate of Evans and Scalliet (1997) of $\Delta FMQ + 2.2$ ($\Delta NNO + 1.7$) at 780 °C was used. Where no oxide pairs were available, fO_2 was estimated using the amphibole oxybarometer of Ridolfi et al. (2010; Kneeling Nun Tuff), or the zircon oxybarometer of Loucks et al. (2020; Peach Springs; Highland Range). Temperature estimates were made using the Ti-in-zircon thermometer of Ferry and Watson (2007) with $a_{TiO_2} = 0.7$ and $a_{SiO_2} = 1$. Zircon data sources: Bishop (Reid et al., 2011), Pinatubo (Lu et al., 2016); Kneeling Nun (Szymanowski et al., 2017), Highland Range (Colombini, 2009); Fish Canyon (Lu et al., 2016; Nathwani et al., 2021), and Peach Springs (Pamukcu et al., 2013).

pendent estimates of oxidation state indicate an increase in oxidation state during crystallisation, this is insufficient to explain the increase in Ce/Nd_{zrc} (Fig. 12). Here, we explore how other parameters in hydrous oxidised magmas – water and phenocryst assemblage – may influence Ce anomalies in zircon.

Increased water activity, lower temperature, and higher $f\text{O}_2$ in felsic melts stabilise titanite at the expense of ilmenite (see Kohn, 2017) and amphibole over pyroxene (e.g., Blatter et al., 2017). Apatite is also a ubiquitous phase in felsic melts irrespective of the water content or oxygen fugacity (Harrison and Watson, 1983). In our model, we emphasise the role of titanite over amphibole or apatite because, despite its low abundance in many magmas, titanite has the greatest potential to significantly increase the Ce/Nd_{melt} ratio. Individual partition coefficients for REEs in titanite are extremely high (D_{Ce} and $D_{\text{Nd}} = 223$ and 639 respectively; Bachmann et al., 2005) and, although amphibole may be an order of magnitude more abundant than titanite in many felsic arc magmas (e.g., Bachmann et al., 2002), its partition coefficients are approximately two orders of magnitude lower, meaning titanite can have close to an order of magnitude greater levering effect on melt compositions than amphibole. Apatite is present in similar abundances to titanite, but its partition coefficients are significantly lower (D_{Ce} and $D_{\text{Nd}} = 48$ and 77 respectively; Sano et al., 2002), and the $D_{\text{Ce}}/D_{\text{Nd}}$ value closer to unity means apatite is less efficient at fractionating Nd from Ce.

To demonstrate the importance of titanite in controlling Ce/Nd_{melt}, we modelled the evolution of the Fish Canyon residual melts by Rayleigh fractional crystallisation of the phenocrysts, both with and without titanite (Fig. 13; see Appendix for model details). Although the titanite-absent models show a modest increase in residual melt Ce/Nd due to the presence of amphibole and apatite in the crystallising assemblage, only with the onset of titanite crystallisation can the high Ce/Nd values observed in the interstitial glass be attained, despite the late onset of titanite crystallisation. Under such conditions, the modest crystallisation of titanite can have a disproportionately large effect on melt composition which can be inherited by zircon and even by subsequent titanite crystals which may be expected to have higher Ce/Nd ratios (e.g., Olson et al., 2017). Although the presence of titanite itself can be considered evidence for the oxidised state of magmas, small changes in $f\text{O}_2$ could lead to large changes in Ce/Nd_{zrc} if titanite saturates as a result. The Ce/Nd_{zrc} ratio depends on the relative timing of titanite saturation and its abundance, and the nature of other phases in the crystallising assemblage. For example, igneous rocks with very high amphibole abundance (e.g., appinites; Murphy, 2013) may also see elevated Ce/Nd_{melt} which may be inherited by co-crystallising zircons.

The suppression of the granite solidus with increasing water content allows the crystallisation of zircon to much lower temperatures (~680 °C at 200 MPa; Johannes and Holtz, 1996) where $D_{\text{Ce}^{4+}}^{\text{zrc}}$ is much higher, which also accounts for larger positive Ce anomalies in zircon. This requires water-saturated conditions, which is also an assumption of our model that we consider to be reasonable.

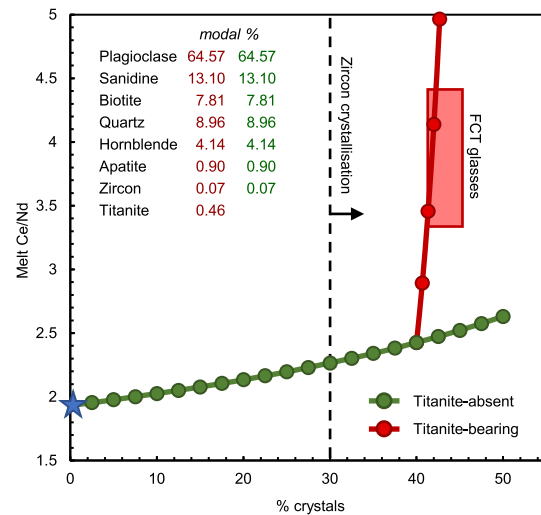


Fig. 13. Rayleigh fractionation modelling of the residual melt Ce/Nd ratio in the Fish Canyon Tuff (FCT) magmas. The models consider the evolution of the residual melt from a bulk rock starting composition (blue star) due to the crystallisation of the phenocryst assemblage (inset). Two scenarios are considered - crystallisation of the phenocryst assemblage without titanite (green line), and with late-stage titanite saturation (red line). The titanite-bearing model commences when the crystal content reaches 40%, which is the approximate crystallinity of a dacite magma at 775 °C, the titanite saturation temperature of the FCT (Szymowski et al., 2017). Similarly, the onset of zircon crystallisation is at ~815 °C, the highest Ti-in-zircon temperature (Fig. 12c); this is equivalent to 30% crystals (crystallinity-temperature estimates from experiments on equivalent dacite magmas; Holtz et al., 2005). Only the titanite bearing model is able to reproduce the interstitial glass Ce/Nd ratio for the appropriate crystallinity (pink rectangle), highlighting the importance of titanite in controlling the Ce/Nd ratio of residual melts and co-crystallising zircons. See Appendix for a full model description.

Experimental estimates show that ~75% crystallisation of a mafic parent is required to generate the dacitic compositions in which zircon typically saturates (Sisson and Grove, 1993; Marxer and Ulmer, 2019). Given that mafic arc magmas – including those parental to evolved porphyry magmas – typically contain ~4 wt.% water (Plank et al., 2013; Chiaradia, 2020), reaching water saturation at 200 MPa (6 wt.% H₂O) would require the fractional crystallisation of only ~35% of the mafic parent magma, assuming that water is mostly incompatible in the crystallising assemblage (10% amphibole in an otherwise anhydrous assemblage yields a bulk $D_{\text{H}_2\text{O}} = 0.05$). This suggests that arc magmas likely achieve water saturation in advance of crystallising zircon, which is supported by the presence of vapour bubbles in zircon-hosted melt inclusions rehomogenised at upper crustal pressures (Thomas et al., 2003). Given that the saturation of zircon is insensitive to melt water content (Boehnke et al., 2013), the water-induced suppression of the granite solidus also implies a more protracted period of zircon crystallisation, allowing it to record an extended period of melt evolution.

Oxybarometric estimates for porphyry magmas including Resolution (Fig. 6; Loucks et al., 2020) suggest that

for the period of magma evolution recorded by zircon, porphyry magmas are likely to exist within the sulphide-sulphate transition, which occurs within 2 log units above the FMQ buffer at 200 MPa (Jugo et al., 2010). This is supported by the presence of sulphide and/or sulphate phases trapped in igneous minerals from porphyry-related magmas (e.g., Stavast et al., 2006; Chambefort et al., 2013) and the decrease in whole rock Cu concentration, indicating sulphide fractionation (e.g., Audéat and Pettke, 2006). Consequently, sulphide saturation in porphyry magmas may not have a deleterious effect on ore-forming potential (e.g., Du and Audéat, 2020) and it has been speculated that this process may increase the size and/or likelihood of porphyry ore deposit formation if concentrated Cu-rich sulphides can be effectively scavenged by subsequent pulses of magma or fluid (Wilkinson, 2013). The observation that ratios of metals in magmatic sulphide inclusions (e.g., Cu/Au) are like those of the metal content of porphyry deposits themselves (Halter et al., 2002), and the presence of partially resorbed and oxidised magmatic sulphides in related igneous rocks (Stavast et al., 2006; Nadeau et al., 2010), are permissive of such a process.

Small, localised fluctuations in oxidation state triggered by degassing of SO₂ (Dilles et al., 2015) or crystallisation of Fe-rich phases (Jenner et al., 2010) are likely to occur, but these processes may be below the resolution of current oxybarometers. In any case, the requirement that porphyry magmas are especially oxidised during magma differentiation is not supported by the observed chemical, petrological, or oxybarometric evidence. Here, we further show that increasingly large Ce anomalies in zircons from porphyry magmas – widely used to support these supposed changes in oxidation state – can be explained more simply by cooling and melt fractionation.

5. CONCLUSIONS

Variations in the magnitude of positive Ce anomalies in zircons from igneous rocks are often interpreted to reflect variations in magma oxidation state. In this paper, we demonstrate that increases in Ce anomalies may occur as a natural consequence of cooling magmas at constant melt redox conditions. Although positive Ce anomalies in zircon are larger in more oxidised melts, our models show that reproducing high zircon Ce/Nd values observed in zircons from oxidised magmas requires a combination of both an increase in melt Ce/Nd and low temperatures, which we show can be a consequence of titanite crystallisation under water-saturated conditions. Given the complexity of Ce partitioning into zircon, we caution against interpreting zircon Ce anomalies solely in the context of melt oxygen fugacity, especially in circumstances where melt chemistry and/or temperature are poorly constrained.

Declaration of Competing Interest

The authors declare that they have no known competing financial interests or personal relationships that could have appeared to influence the work reported in this paper.

ACKNOWLEDGEMENTS

This paper is derived from the lead author's PhD research, which was fully funded by Rio Tinto Exploration (Imperial Project P34899). We thank Paul Agnew, Alan Kobussen, Hamish Martin, Carl Hehnke, and Alan Seymour for assistance and input into this work, and we are grateful to Resolution Copper LLC for permission to publish. The assistance of Anton Kearsley, John Spratt, and Teresa Jeffries with laboratory work is gratefully acknowledged. We thank our colleagues from the London Centre for Ore Deposits and Exploration (LODE) who provided useful insights during the preparation of this manuscript. This paper also benefited from useful comments by John Dilles and two anonymous reviewers. CN was supported by the Natural Environment Research Council via a Science and Solutions for a Changing Planet doctoral studentship (grant NE/L002515/1) at Imperial College London and Anglo American. JW acknowledges funding under Natural Environment Research Council grant (NE/P017452/1) "From arc magmas to ores (FAMOS): A mineral systems approach". ML was supported by BHP Minerals during the writing of the manuscript.

APPENDIX A. SUPPLEMENTARY MATERIAL

Supplementary material to this article can be found online at <https://doi.org/10.1016/j.gca.2022.03.024>.

REFERENCES

- Aigner-Torres M., Blundy J., Ulmer P. and Pettke T. (2007) Laser Ablation ICPMS study of trace element partitioning between plagioclase and basaltic melts: an experimental approach. *Contrib. Mineral. Petr.* **153**, 647–667.
- Audéat A. and Pettke T. (2006) Evolution of a Porphyry-Cu Mineralized Magma System at Santa Rita, New Mexico (USA). *J. Petrol.* **47**, 2021–2046.
- Bachmann O., Dungan M. A. and Lipman P. W. (2002) The Fish Canyon Magma Body, San Juan Volcanic Field, Colorado: Rejuvenation and Eruption of an Upper-Crustal Batholith. *J. Petrol.* **43**, 1469–1503.
- Bachmann O., Dungan M. A. and Bussy F. (2005) Insights into shallow magmatic processes in large silicic magma bodies: the trace element record in the Fish Canyon magma body, Colorado. *Contrib. Mineral. Petr.* **149**, 338–349.
- Ballard J., Palin M. and Campbell I. (2002) Relative oxidation states of magmas inferred from Ce(IV)/Ce(III) in zircon: application to porphyry copper deposits of northern Chile. *Contrib. Mineral. Petr.* **144**, 347–364.
- Blatter D., Sisson T. and Hankins W. (2017) Voluminous arc dacites as amphibole reaction-boundary liquids. *Contrib. Mineral. Petr.* **172**, 1–37.
- Blundy J. D. and Wood B. J. (1994) Prediction of crystal-melt partition coefficients from elastic moduli. *Nature* **372**, 452–454.
- Boehnke P., Watson B. E., Trail D., Harrison T. M. and Schmitt A. K. (2013) Zircon saturation re-revisited. *Chem. Geol.* **351**, 324–334.
- Burnham A. and Berry A. (2012) An experimental study of trace element partitioning between zircon and melt as a function of oxygen fugacity. *Geochim. Cosmochim. Acta* **95**, 196–212.
- Burnham A. and Berry A. (2014) The effect of oxygen fugacity, melt composition, temperature and pressure on the oxidation state of cerium in silicate melts. *Chem. Geol.* **366**, 52–60.
- Burnham A., Berry A., Halse H., Schofield P., Cibin G. and Mosselmans J. (2015) The oxidation state of europium in

- silicate melts as a function of oxygen fugacity, composition and temperature. *Chem. Geol.* **411**, 248–259.
- Carmichael I. (1991) The redox states of basic and silicic magmas: a reflection of their source regions? *Contrib. Mineral. Petr.* **106**, 129–141.
- Cicconi M., Le Losq C., Henderson G. and Neuville N. (2021) The Redox Behavior of Rare Earth Elements. In *Magma Redox Geochemistry. Geophysical Monograph Series*. Wiley, pp. 381–398.
- Chambefort I., Dilles J. H. and Longo A. A. (2013) Amphibole geochemistry of the Yanacocha volcanics, Peru: Evidence for diverse sources of magmatic volatiles related to gold ores. *J. Petrol.* **54**, 1017–1046.
- Chamberlain K., Wilson C., Wallace P. and Millet M. (2015) Micro-analytical Perspectives on the Bishop Tuff and its Magma Chamber. *J. Petrol.* **56**, 605–640.
- Chiariadis M. (2020) How much water in basaltic melts parental to porphyry copper deposits? *Front. Earth Sci.* **8**, 138.
- Chelle-Michou C., Chiariadis M., Ovtcharova M., Ulianov A. and Wotzlaw J. (2014) Zircon petrochronology reveals the temporal link between porphyry systems and the magmatic evolution of their hidden plutonic roots (the Eocene Corocochuayco deposit, Peru). *Lithos* **198–199**, 129–140.
- Cherniak D. and Watson E. (2003) Diffusion in zircon. *Rev. Mineral. Geochem.* **53**, 113–143.
- Claiborne L. L., Miller C. F., Gualda G. A., Carley T. L., Covey A. K., Wooden J. L. and Fleming M. A. (2018) Zircon as magma monitor: robust, temperature-dependent partition coefficients from glass and zircon surface and rim measurements from natural systems. In *Microstructural Geochronology: Planetary Records Down to Atom Scale. Geophysical Monograph Series*, 232 (ed. Moser). AGU Books, Washington DC, USA, pp. 1–33.
- Colombini L. (2009) *Mid-Miocene rhyolite sequence, Highland Range, NV: record of magma evolution and eruption from the Searchlight pluton magma chamber* MSc Thesis. Vanderbilt University.
- Colombini L., Miller C., Gualda G., Wooden J. and Miller J. (2011) Sphene and zircon in the Highland Range volcanic sequence (Miocene, southern Nevada, USA): elemental partitioning, phase relations, and influence on evolution of silicic magma. *Mineral. Petrol.* **102**, 29–50.
- Davis D., Williams I. and Krogh T. (2003) Historical development of zircon geochronology. *Rev. Mineral. Geochem.* **53**, 145–181.
- Dilles J. H., Kent A. J. R., Wooden J. L., Tosdal R. M., Koleszar A., Lee R. G. and Farmer L. P. (2015) Zircon compositional evidence for sulfur-degassing from ore-forming arc magmas. *Econ. Geol.* **110**, 241–251.
- Du J. and Audétat A. (2020) Early sulfide saturation is not detrimental to porphyry Cu-Au formation. *Geology* **48**, 519–524.
- Evans B. and Scalliet B. (1997) The redox state of Pinatubo dacite and the ilmenite-hematite solvus. *American Mineralogist* **85**(5–6), 625–629.
- Ferry J. and Watson E. (2007) New thermodynamic models and revised calibrations for the Ti-in-zircon and Zr-in-rutile thermometers. *Contrib. Mineral. Petrol.* **154**, 429–437.
- Ghiorso M. S. and Evans B. W. (2008) Thermodynamics of Rhombohedral Oxide Solid Solutions and a Revision of the Fe-Ti Two-Oxide Geothermometer and Oxygen-Barometer. *Am. J. Sci.* **308**, 957–1039.
- Grove T. L., Donnelly-Nolan J. M. and Housh T. (1997) Magmatic processes that generated the rhyolite of Glass Mountain, Medicine Lake volcano, N. California. *Contributions to Mineralogy and Petrology* **127**, 205–223.
- Halter W. E., Pettke T. and Heinrich C. A. (2002) The Origin of Cu/Au Ratios in Porphyry-Type Ore Deposits. *Science* **296**, 1844–1846.
- Harrison T. M. and Watson E. B. (1983) Kinetics of zircon dissolution and zirconium diffusion in granitic melts of variable water-content. *Contrib. Mineral. Petrol.* **84**, 66–72.
- Hehnke C., Ballantyne G., Martin H., Hart W., Schwartz A. and Stein H. (2012) Geology and Exploration Progress at the Resolution porphyry Cu-Mo deposit, Arizona. *Soc. Econ. Geol. Spec. P.* **16**, 147–166.
- Hildreth W. and Wilson C. J. N. (2007) Compositional zoning of the Bishop Tuff. *J. Petrol.* **48**, 951–999.
- Hildreth W. (1979) The Bishop Tuff: Evidence for the origin of compositional zonation in silicic magma chambers. *Geol. S. Am. S.* **180**, 43–75.
- Holtz F., Hiroaki S., Lewis J., Behrens H. and Nakada S. (2005) Experimental Petrology of the 1991–1995 Unzen Dacite, Japan. Part I: Phase Relations, Phase Composition and Pre-eruptive Conditions. *J. Petrol.* **46**, 319–337.
- Hoskin P. and Schaltegger U. (2003) The composition of zircon and igneous and metamorphic petrogenesis. *Rev. Mineral. Geochem.* **53**, 27–62.
- Jenner F., O'Neill H., Arculus R. and Mavrogenes J. (2010) The Magnetite Crisis in the Evolution of Arc-related Magmas and the Initial Concentration of Au, Ag and Cu. *J. Petrol.* **51**, 2445–2464.
- Johannes W. and Holtz F. (1996) *Petrogenesis and Experimental Petrology of Granitic Rocks*. Springer Verlag, Berlin.
- Johnson M. C. and Rutherford M. J. (1989) Experimental calibration of the aluminum-in-hornblende geobarometer with application to Long Valley caldera (California) volcanic rocks. *Geology* **17**(9), 837–841.
- Jugo P., Wilke M. and Botcharnikov R. (2010) Sulfur K-edge XANES analysis of natural and synthetic basaltic glasses: Implications for S speciation and S content as function of oxygen fugacity. *Geochim. Cosmochim. Acta* **74**, 5926–5938.
- Klimm K., Blundy J. D. and Green T. H. (2008) Trace element partitioning and accessory phase saturation during H₂O-saturated melting of basalt with implications for subduction zone chemical fluxes. *J. Petrol.* **49**, 523–553.
- Kobylinski C., Hattori K., Smith S. and Plouffe A. (2020) Protracted magmatism and mineralized hydrothermal activity at the Gibraltar porphyry copper-molybdenum deposit, British Columbia. *Econ. Geol.* **115**, 1119–1136.
- Kohn M. (2017) Titanite petrochronology. *Rev. Mineral. Geochem.* **83**, 419–441.
- Lang J. and Titley S. (1998) Isotopic and geochemical characteristics of Laramide magmatic systems in Arizona and implications for the genesis of porphyry copper deposits. *Econ. Geol.* **93**, 138–170.
- Loader M. A. (2017) *Mineral Indicators of Porphyry Cu Fertility*. Ph. D. thesis. Imperial College London.
- Loader M. A., Wilkinson J. and Armstrong R. (2017) The effect of titanite crystallisation on Eu and Ce anomalies in zircon and its implications for the assessment of porphyry Cu deposit fertility. *Earth Planet. Sc. Lett.* **472**, 107–119.
- Loucks R. R. (2014) Distinctive composition of copper-ore-forming arc magmas. *Aust. J. Earth Sci.* **61**, 5–16.
- Loucks R. R., Fiorentini M. L. and Rohrlach B. (2018) Divergent T-fO₂ paths during crystallisation of H₂O-rich and H₂O-poor magmas as recorded by Ce and U in zircon, with implications for TitaniQ and TitaniZ geothermometry. *Contrib. Mineral. Petrol.* **173**, 1–21.
- Loucks R. R., Fiorentini M. L. and Henríquez G. (2020) New Magmatic Oxybarometer Using Trace Elements in Zircon. *J. Petrol.* **61**.
- Lu Y.-J., Loucks R. R., Fiorentini M., McCuaig T. C., Evans N. J., Yang Z.-M., Hou Z.-Q., Kirkland C. L., Parra-Avila L. A. and Kobussen A. (2016) Zircon Compositions as a Pathfinder for

- Porphyry Cu ± Mo ± Au Deposits. *Soc. Econ. Geol. Spec. P.* **19**, 329–347.
- Luo Y. and Ayers J. (2009) Experimental measurements of zircon/melt trace-element partition coefficients. *Geochim. Cosmochim. Acta* **73**, 3656–3679.
- Marshall A. S., MacDonald R., Rogers N. W., Fitton J. G., Tindle A. G., Nejbert K. and Hinton R. W. (2009) Fractionation of Peralkaline Silicic Magmas: the Greater Olkaria Volcanic Complex, Kenya Rift Valley. *J. Petrol.* **50**, 323–359.
- Martel C., Pichavant M., Holtz F., Scalliet B., Bourdier J. L. and Trainea H. (1999) Effects of $f\text{O}_2$ and H_2O on andesite phase relations between 2 and 4 kbar. *Journal of Geophysical Research: Solid Earth* **104**, 29453–29470.
- Marxer F. and Ulmer P. (2019) Crystallisation and zircon saturation of calc-alkaline tonalite from the Adamello Batholith at upper crustal conditions: an experimental study. *Contrib. Mineral. Petr.* **174**, 1–29.
- Moore G. and Carmichael I. S. E. (1998) The hydrous phase equilibria (to 3 kbar) of an andesite and basaltic andesite from western Mexico: constraints on water content and conditions of phenocryst growth. *Contributions to Mineralogy and Petrology* **130**, 304–319.
- Morton A., Waters C., Fanning M., Chisholm I. and Brettle M. (2015) Origin of Carboniferous sandstones fringing the northern margin of the Wales-Brabant Massif: insights from detrital zircon ages. *Geol. J.* **50**, 553–574.
- Murphy J. (2013) Appinite suites: A record of the role of water in the genesis, transport, emplacement and crystallization of magma. *Earth Sci. Rev.* **119**, 35–59.
- Nadeau O., Williams-Jones A. E. and Stix J. (2010) Sulphide Magma as a Source of Metals in Arc-Related Magmatic Hydrothermal Ore Fluids. *Nat. Geosci.* **3**, 501–505.
- Nandedkar R., Hürlmann N., Ulmer P. and Müntener O. (2016) Amphibole-melt trace element partitioning of fractionating calc-alkaline magmas in the lower crust: an experimental study. *Contrib. Mineral. Petr.* **171**, 1–25.
- Nathwani C., Simmons A., Large S., Wilkinson J., Buret Y. and Ihlenfeld C. (2021) From long-lived batholith construction to giant porphyry copper deposit formation: petrological and zircon chemical evolution of the Quellaveco District, Southern Peru. *Contrib. Mineral. Petr.* **176**.
- Newman S. and Lowenstern J. B. (2002) VolatileCalc: a silicate melt- H_2O - CO_2 solution model written in visual basic for excel. *Comput. Geosci.* **28**, 597–604.
- Olson N. H., Dilles J. H., Kent A. J. R. and Lang J. R. (2017) Geochemistry of the Cretaceous Kaskanak Batholith and genesis of the Pebble porphyry Cu-Au-Mo deposit, Southwest Alaska. *Am. Min.* **102**(8), 1597–1621.
- Padilla A. and Gualda G. (2016) Crystal-melt elemental partitioning in silicic magmatic systems: An example from the Peach Spring Tuff high-silica rhyolite, Southwest USA. *Chem. Geol.* **440**, 326–344.
- Pamukcu A., Carley T., Gualda G., Miller C. and Ferguson C. (2013) The Evolution of the Peach Spring Giant Magma Body: Evidence from Accessory Mineral Textures and Compositions, Bulk Pumice and Glass Geochemistry, and Rhyolite-MELTS Modeling. *J. Petrol.* **54**, 1109–1148.
- Patten C., Barnes S., Mathez E. and Jenner F. (2013) Partition coefficients of chalcophile elements between sulfide and silicate melts and the early crystallization history of sulfide liquid: LA-ICP-MS analysis of MORB sulfide droplets. *Chem. Geol.* **358**, 170–188.
- Pizarro H., Campos E., Bouzari F., Rousse S., Bissig T., Gregoire M. and Riquelme R. (2020) Porphyry indicator zircons (PIZs): Application to exploration of porphyry copper deposits. *Ore Geol. Rev.* **126**, 103771.
- Plank T., Kelley K., Zimmer M., Hauri E. and Wallace P. (2013) Why do mafic arc magmas contain ~4wt% water on average? *Earth Planet. Sc. Lett.* **364**, 168–179.
- Reid M., Vazquez J. and Schmitt A. (2011) Zircon-scale insights into the history of a Supervolcano, Bishop Tuff, Long Valley, California, with implications for the Ti-in-zircon geothermometer. *Contrib. Mineral. Petr.* **161**, 293–311.
- Rezeau H., Moritz R., Wotzlaw J., Hovakimyan S. and Tayan R. (2019) Zircon petrochronology of the Meghri-Ordubad Pluton, Lesser Caucasus; fingerprinting igneous processes and implications for the exploration of porphyry Cu-Mo deposits. *Econ. Geol.* **114**, 1365–1388.
- Richards J. (2011) High Sr/Y arc magmas and porphyry Cu ± Mo ± Au deposits; just add water. *Econ. Geol.* **106**, 1075–1081.
- Ridolfi F., Renzulli A. and Puerini M. (2010) Stability and chemical equilibrium of amphibole in calc-alkaline magmas: an overview, new thermobarometric formulations and application to subduction-related volcanoes. *Contrib. Mineral. Petr.* **160**, 45–66.
- Rutherford M. J. and Devine J. D. (2003) Magmatic conditions and magma ascent as indicated by hornblende phase equilibria and reactions in the 1995–2002 Soufrière Hills magma. *Journal of Petrology* **44**, 1433–1454.
- Rutherford M., Sigurdsson H., Carey S. and Davis A. (1985) The May 18, 1980, Eruption of Mount St. Helens: 1. Melt composition and Experimental Phase Equilibria. *Journal of Geophysical Research* **90**(B4), 2929–2947.
- Sano Y., Terada K. and Fukuoka T. (2002) High mass resolution ion microprobe analysis of rare earth elements in silicate glass, apatite and zircon: lack of matrix dependency. *Chem. Geol.* **184**, 217–230.
- Schopä A., Annen C., Dilles J. H., Sparks R. S. J. and Blundy J. D. (2017) Magma emplacement rates and porphyry copper deposits: thermal modelling of the Yerington Batholith, Nevada. *Econ. Geol.* **112**, 1653–1672.
- Seedorff E., Dilles J. H., Proffett, Jr., J. M., Einaudi M. T., Zurcher L., Stavast W. J. A., Johnson D. A. and Barton M. D. (2005) Porphyry deposits: Characteristics and origin of hypogene features. *Econ. Geol.* **100**, 251–298.
- Seedorff E., Barton M. D., Gehrels G. E., Valencia V. A., Johnson D. A., Maher D. J., Stavast W. J. and Marsh T. M. (2019) Temporal evolution of the Laramide arc: U-Pb geochronology of plutons associated with porphyry copper mineralization in east-central Arizona. *Geol. Soc. Am. Field Guide* **55**, 369–400.
- Shen P. S., Hattori K., Pan H. P., Jackson S. and Seitmuratova E. (2015) Oxidation condition and metal fertility of granitic magmas: zircon trace-element data from porphyry Cu deposits in the Central Asian orogenic belt. *Econ. Geol.* **110**, 1861–1878.
- Sillitoe R. H. (2010) Porphyry copper systems. *Econ. Geol.* **105**, 3–41.
- Sisson T. and Grove T. (1993) Experimental investigations of the role of H_2O in calc-alkaline differentiation and subduction zone magmatism. *Contrib. Mineral. Petr.* **113**, 143–166.
- Smythe D. J. and Brenan J. M. (2015) Cerium oxidation state in silicate melts: Combined $f\text{O}_2$, temperature and compositional effects. *Geochim. Cosmochim. Acta* **170**, 173–187.
- Smythe D. J. and Brenan J. M. (2016) Magmatic oxygen fugacity estimated using zircon-melt partitioning of cerium. *Earth Planet. Sc. Lett.* **453**, 260–266.
- Stavast W., Keith J., Christiansen E., Dorais M., Tingey D., Larocque A. and Evans N. (2006) The fate of magmatic sulfides during intrusion or eruption, Bingham and Tintic districts, Utah. *Econ. Geol.* **101**, 329–345.

- Sun S. S. and McDonough W. F. (1989) Chemical and isotopic systematics of oceanic basalts: implications for mantle composition and processes. *Geol. Soc. Spec. P.* **42**, 313–345.
- Sun W., Huang R., Li H., Hu Y., Zhang C., Sun S., Zhang L., Ding X., Li C., Zartman R. and Ling M. (2015) Porphyry deposits and oxidized magmas. *Ore Geol. Rev.* **65**, 97–131.
- Szymanowski D., Wotzlaw J., Ellis B., Bachmann O., Guillong M. and von Quadt A. (2017) Protracted near-solidus storage and pre-eruptive rejuvenation of large magma reservoirs. *Nat. Geosci.* **10**, 777–782.
- Thomas J., Bodnar R., Shimizu N. and Chesner C. (2003) Melt inclusions in zircon. *Rev. Mineral. Geochem.* **51**, 63–87.
- Trail D., Watson E. and Tailby N. (2012) Ce and Eu anomalies in zircon as proxies for the oxidation state of magmas. *Geochim. Cosmochim. Acta* **97**, 70–87.
- Viala M. and Hattori K. (2021) Hualgayoc mining district, northern Peru: Testing the use of zircon composition in exploration for porphyry-type deposits. *J. Geochem. Explor.* **223**, 106725.
- Whitney J. A. and Stormer J. C. (1985) Mineralogy, petrology, and magmatic conditions from the Fish Canyon Tuff, central San Juan volcanic field, Colorado. *J. Petrol.* **26**, 726–762.
- Wilke M. and Behrens H. (1999) The dependence of the partitioning of iron and europium between plagioclase and hydrous tonalitic melt on oxygen fugacity. *Contrib. Mineral. Petr.* **137**, 102–114.
- Wilkinson J. (2013) Triggers for the formation of porphyry ore deposits in magmatic arcs. *Nat. Geosci.* **6**, 917–925.
- Wotzlaw J., Schaltegger U., Frick D., Dungan M., Gerdes A. and Günther D. (2013) Tracking the evolution of large-volume silicic magma reservoirs from assembly to supereruption. *Geology* **41**, 867–870.
- Zacharias J. and Wilkinson J. J. (2007) ExLAM 2000: Excel VBA application for processing of transient signal data from laser ablation (LA-ICP-MS) of fluid inclusions and solid phases. In *ECROFI-XIX Abs. vol.*, p. 194.
- Zhong S., Seltmann R., Qu H. and Song Y. (2019) Characterization of the zircon Ce anomaly for estimation of oxidation state of magmas: a revised Ce/Ce method. *Mineral. Petrol.* **113**, 755–763.

Associate editor: Weidong Sun